remote sensing

Article

# Research on Mass Center Identification for Gravitational Wave Detection Spacecraft with Guaranteed Laser Link Pointing Accuracy

**Shen-Ao Wang [1], Huibo Zhang [2,*], Lin Cai [3], Ziming Wang [4] and Yumin An [2]**

1 School of Mechanical Engineering, Hebei University of Technology, Tianjin 300401, China; 202321202124@stu.hebut.edu.cn
2 College of Mechanical and Electrical Engineering, Harbin Engineering University, Harbin 150001, China; anyumin@hebut.edu.cn
3 School of Physics, Huazhong University of Science and Technology, Wuhan 430074, China; cailin@hust.edu.cn
4 School of Astronautics, Harbin Institute of Technology, Harbin 150001, China; 24b918118@stu.hit.edu.cn
* Correspondence: zhanghuibo@hrbeu.edu.cn

**Abstract:** The deviation of the center of mass of a gravitational wave detection satellite from its calibrated position can severely impact the accuracy of gravitational wave detection. Therefore, there is an urgent need to develop effective identification methods to achieve precise center of mass identification while ensuring the alignment of the laser link. To address this issue, this paper proposes a method for the center of mass identification of gravitational wave detection spacecraft that ensures the pointing accuracy of the laser link. A study on the relative attitude dynamics modeling of gravitational wave detection spacecraft is conducted, and the conditions for small, periodic spacecraft maneuvers that maintain laser link alignment are analyzed. A high-precision, high-stability center of mass identification method based on dual-model data fusion is proposed and simulated. The results show that this method can maintain the alignment precision of the laser interferometer arms within 10 nrad, while achieving a center of mass identification accuracy of 25 μm. Compared to existing methods, this method improves the identification accuracy by an order of magnitude, demonstrating its feasibility for application in gravitational wave detection constellations. It provides theoretical support for the center of mass identification of gravitational wave detection spacecraft.

**Keywords:** gravitational wave detection spacecraft; spacecraft dynamics model; laser link directivity; center of mass identification

check for updates

Academic Editor: Jianguo Yan

Received: 11 December 2024
Revised: 9 January 2025
Accepted: 13 January 2025
Published: 15 January 2025

**Citation:** Wang, S.-A.; Zhang, H.; Cai, L.; Wang, Z.; An, Y. Research on Mass Center Identification for Gravitational Wave Detection Spacecraft with Guaranteed Laser Link Pointing Accuracy. *Remote Sens.* **2025**, *17*, 296. https://doi.org/10.3390/rs17020296



## 1. Introduction

In space-based gravitational wave detection missions, achieving ultra-precise, ultra-stable, and ultra-steady center of mass (COM) identification of spacecraft remains a challenging issue. This requires that, under scientific observation mode, the residual acceleration noise of the test mass along the sensitive axis should be below $10^{-15}/\mathrm{s}^2/\mathrm{Hz}^{1/2}$ [1–3], the displacement measurement noise should be below 1 $\mathrm{pm}/\mathrm{Hz}^{1/2}$ [4,5], and the laser link angular deviation should be smaller than 10 nrad [6,7]. Ideally, the COM of the spacecraft should coincide with that of the test mass. However, after prolonged on-orbit operation, the gravitational wave detection spacecraft is affected by factors such as fuel consumption and structural thermal deformation, which can cause its COM to deviate from the calibrated position [8,9]. When the spacecraft's COM shifts, measurement errors are introduced. The accelerometer will not only measure the non-conservative force acceleration but also the perturbation acceleration caused by the COM deviation. This significantly increases the acceleration noise along the sensitive axis of the test mass, severely impacting the gravitational wave detection mission [10,11]. Therefore, it is crucial to periodically identify the spacecraft's COM position in order to adjust the relative positioning of the spacecraft and the test mass, ensuring that their COMs remain coincident.

Many researchers have conducted studies on the identification of spacecraft's mass property. Huang et al. [12] investigated center of mass (COM) identification for the GRACE satellite, establishing an observation equation composed of accelerometer measurement equations. By applying periodic excitation signals to the magnetorquers to induce spacecraft maneuvers, they obtained four different types of COM offset results using four different angular accelerations. A comparison of the COM offset estimates from these four methods showed that the accuracy of all results was at the same level, with a deviation of 0.5 μm from the JPL estimates, while traditional methods had a deviation of 6 μm from the JPL results. However, their study did not take into account the laser alignment issue for gravity satellites, and the identification process was not conducted under the premise of ensuring laser link pointing stability, making it unsuitable for space-based gravitational wave detection missions.

Wei et al. [13] proposed a new identification method for the on-orbit COM identification of the Tianhyi-1 satellite. They established an observation equation based on an accelerometer model and estimated the COM deviation using an extended Kalman filter combined with a Rauch–Tung–Striebel smoother. A chi-square test was introduced to eliminate outliers, and a nonlinear least squares algorithm was used for cross-validation. The results showed that $dx \approx -0.19$ mm, $dy \approx 0.64$ mm, and $dz \approx -0.82$ mm, which did not meet the micron-level accuracy required for spacecraft. Although Wei et al. [13] addressed error processing in their identification process, they did not consider the laser link alignment issue and did not specify the maneuvering method used for the spacecraft during the identification process.

Li [14] conducted a study on COM position identification for gravity satellites using batch estimation theory and Kalman filtering algorithms. The simulation results indicated that during the COM calibration maneuvers induced by the magnetorquers, the calibration accuracy of the COM could reach 100 μm. However, this accuracy does not meet the COM calibration requirements for gravitational wave detection satellites.

Building upon Li's research, Wang [15] and Xin [16] proposed an algorithm for estimating spacecraft COM position using both accelerometers and gyroscopes. They combined Kalman filtering with predictive filtering, using the spacecraft's angular acceleration and COM offset as state estimators to estimate the spacecraft's angular acceleration and COM offset in real time. However, this method assumes that the spacecraft's moment of inertia and mass are inaccurate and uses predictive filtering to estimate angular acceleration, which increases complexity. Additionally, it does not align with the reality of gravitational wave detection satellites, which require high-precision inertial matrices and mass parameters.

In summary, the main limitation of existing center of mass identification methods is the failure to account for the attitude constraints of the spacecraft during the identification process. During center of mass identification, if scientific exploration mode is exited, it will reduce the spacecraft's observation lifetime. Therefore, it is crucial to keep the laser interferometer arms aligned as much as possible. Re-aligning after disconnecting the link would waste valuable observation time [17,18]. On the other hand, if the impact of attitude maneuvers on the laser link is not considered during the identification process, and if no attitude constraints are applied during the maneuver, the pointing direction of the laser link will be disrupted. This disturbance in the laser light path will introduce acceleration noise, which can negatively affect the gravitational wave detection mission [19,20]. Thus, current research is not applicable to the identification of the center of mass for ultra-precise, ultra-stable, and ultra-steady spacecraft. It fails to address the attitude constraints during the identification process, thus compromising the accuracy of the gravitational wave detection task during center of mass identification.

To address the aforementioned issues, this paper proposes a method for the center of mass (COM) identification of gravitational wave detection spacecraft that ensures laser link pointing stability. A relative motion attitude dynamics equation is established as the foundation for preventing relative displacement between spacecraft and for the attitude controller. An accelerometer measurement model was developed, considering space environmental disturbance factors that could affect the detection task. A constraint domain for spacecraft rotational maneuvers is introduced, based on which the attitude controller is used to control the spacecraft maneuvers. The resulting motion data are collected and analyzed, and appropriate filtering is applied to mitigate the interference from disturbance factors. Subsequently, the COM position is identified using the obtained kinematic data and a least squares algorithm. On the one hand, the proposed method ensures the pointing stability of the laser link during the identification process. On the other hand, it achieves micron-level accuracy in spacecraft COM identification, providing an accurate and reliable data benchmark for subsequent COM control.

## 2. Research on Maneuver Scheme of Spacecraft Center of Mass Identification

### *2.1. Coordinate System*

A space-based gravitational wave detection mission consists of three spacecraft arranged in an equilateral triangle formation. In this study, based on the Tianqin mission, the COM identification problem for the upcoming Tianqin-2 satellite was investigated. Therefore, the focus of this paper is on two gravitational wave detection spacecraft. To describe the relative motion between the two spacecraft, three important spatial coordinate systems are established, as shown in Figure 1.

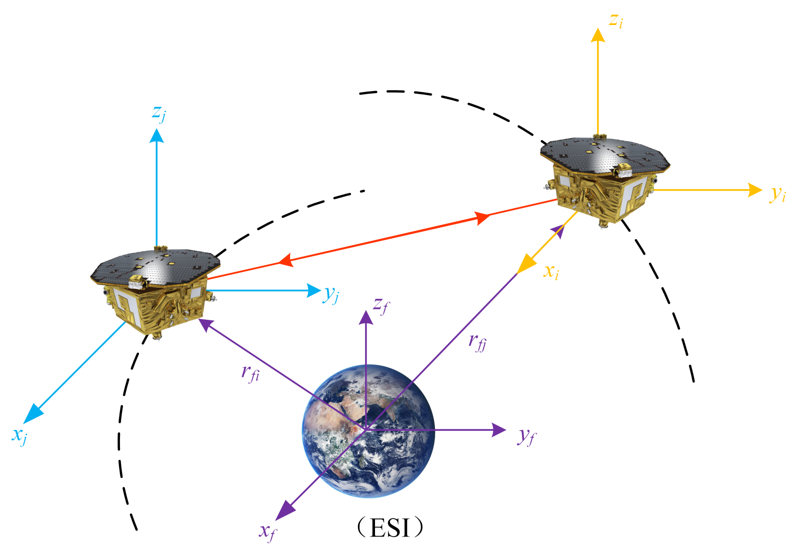


**Figure 1.** Coordinate reference.

(1) Earth's Inertial Reference Frame F ($s_f$)

The origin is located at the center of the Earth. The X-axis points toward the vernal equinox, the Z-axis points toward the North Pole, and the Y-axis lies in the equatorial plane, determined using the right-hand rule.

(2) Primary Spacecraft Body Coordinate System I ($s_i$)

The origin is located at the calibrated center of mass of the spacecraft. The X-axis is directed along the line connecting the center of mass and the laser link, pointing outward.

The Z-axis is perpendicular to the spacecraft's plane, and the Y-axis is determined using the right-hand rule.

(3) Secondary Spacecraft Body Coordinate System J ($s_j$)

This coordinate system is the same as the primary spacecraft's, with the origin at the calibrated center of mass. The X-axis is directed along the line connecting the center of mass and the laser link, pointing outward. The Z-axis is perpendicular to the spacecraft's plane, and the Y-axis is determined using the right-hand rule.

## 2.2. Attitude Constraint Analysis of Spacecraft

### 2.2.1. Kinematics Model of Spacecraft Formation Attitude

The relative attitude between spacecraft is one of the key factors affecting the laser link. Due to disturbing forces, the spacecraft will drift away from the calibrated orbit after a certain period, resulting in relative displacement between the spacecraft. This displacement will prevent interference between the two laser beams, thereby obstructing gravitational wave detection. Therefore, during the COM identification process, a necessary condition for spacecraft maneuvers is to constrain the relative motion between the two spacecraft.

Next, we construct the spacecraft relative motion attitude dynamics model. We assume that the spacecraft is an ideal rigid body and use rigid-body kinematics to describe the relative attitude motion of the spacecraft. Based on the established coordinate systems, the position vector components are represented by xf, yf, and zf in the Earth's inertial reference frame, with their rates of change given by $dx_f/dt$, $dy_f/dt$, and $dz_f/dt$. The spacecraft body coordinate system is denoted by $o_b x_b y_b z_b$.

Define the attitude quaternion of the spacecraft body coordinate system relative to the reference frame as

$$\boldsymbol{q} = \begin{bmatrix} \bar{\boldsymbol{q}}^{\mathrm{T}} & q_4 \end{bmatrix}^{\mathrm{T}} = \begin{bmatrix} q_1 & q_2 & q_3 & q_4 \end{bmatrix}^{\mathrm{T}} \tag{1}$$

The quaternion components are defined as follows: $q_1 = e_1 sin\varphi/2$, $q_2 = e_2 sin\varphi/2$, $q_3 = e_3 sin\varphi/2$, and $q_4 = cos\varphi/2$. Here, $\bar{\boldsymbol{q}} = [q_1, q_2, q_3]^T$ represents the vector part of the quaternion, while q4 represents the scalar part of the quaternion, and is the rotation angle about the Euler axis $\boldsymbol{e} = (e_1, e_2, e_3)^T$.

We define $\otimes$ as the quaternion product:

$$\begin{aligned} \boldsymbol{q}_i \otimes \boldsymbol{q}_j &= \begin{bmatrix} \overline{\boldsymbol{q}}_i^{\times} + q_{i4}\boldsymbol{I}_3 & \overline{\boldsymbol{q}}_i \\ -\overline{q}_i^{\mathrm{T}} & q_{i4} \end{bmatrix} \begin{bmatrix} \overline{\boldsymbol{q}}_j \\ q_{j4} \end{bmatrix} \\ &= \begin{bmatrix} -\overline{\boldsymbol{q}}_j^{\times} + q_{j4}\boldsymbol{I}_3 & \overline{q}_j \\ -\overline{\boldsymbol{q}}_j^{\mathrm{T}} & q_{j4} \end{bmatrix} \begin{bmatrix} \overline{\boldsymbol{q}}_i \\ q_{i4} \end{bmatrix} \end{aligned} \tag{2}$$

The above equation represents a composite rotation resulting from two successive rotations, $q_i$ and $q_j$.

Then, we define the following operation:

$$\begin{aligned} \boldsymbol{\Psi}(\boldsymbol{\xi}) &= \begin{bmatrix} \bar{\boldsymbol{\xi}}^{\times} + \xi_4\boldsymbol{I}_3 & \bar{\boldsymbol{\xi}} \\ -\bar{\boldsymbol{\xi}}^{\mathrm{T}} & \xi_4 \end{bmatrix}, \\ \overline{\boldsymbol{\Psi}}(\boldsymbol{\xi}) &= \begin{bmatrix} -\bar{\boldsymbol{\xi}}^{\times} + \xi_4\boldsymbol{I}_3 & \bar{\boldsymbol{\xi}} \\ -\bar{\boldsymbol{\xi}}^{\mathrm{T}} & \xi_4 \end{bmatrix} \end{aligned} \tag{3}$$

where $\boldsymbol{\Psi}(\boldsymbol{\xi})$, $\overline{\boldsymbol{\Psi}}(\boldsymbol{\xi}) \in R^{4\times4}$, and $\boldsymbol{\xi} = [\bar{\boldsymbol{\xi}}^{\mathrm{T}}\xi_4] = [\xi_1 \cdot \xi_2 \cdot \xi_3 \cdot \xi_4]^{\mathrm{T}}$.

Based on Equations (2) and (3), we can obtain the following:

$$\boldsymbol{q}_i \otimes \boldsymbol{q}_j = \boldsymbol{\Psi}(\boldsymbol{q}_i)\boldsymbol{q}_j = \bar{\boldsymbol{\Psi}}(\boldsymbol{q}_j)\boldsymbol{q}_i \tag{4}$$

From Equation (2), the quaternion product satisfies $\boldsymbol{q} \otimes \boldsymbol{q}^{-1} = [0 \cdot 0 \cdot 0 \cdot 1]^{\mathrm{T}}$. Differentiating this, we obtain

$$\dot{\boldsymbol{q}} \otimes \boldsymbol{q}^{-1} + \boldsymbol{q} \otimes \dot{\boldsymbol{q}}^{-1} = \mathbf{0}_{4\times 1} \tag{5}$$

The expression of the spacecraft kinematic equation in the reference frame, based on the quaternion description, is given by

$$\dot{\boldsymbol{q}} = \frac{1}{2}\bar{\boldsymbol{\Psi}}(\tilde{\boldsymbol{\omega}})\boldsymbol{q} \tag{6}$$

where $\tilde{\boldsymbol{\omega}} = [\boldsymbol{\omega}^{\mathrm{T}}, 0]^{\mathrm{T}}$.

Equation (6) can be expressed as

$$\dot{\boldsymbol{q}} = \frac{1}{2}\boldsymbol{\Psi}(\boldsymbol{q})\tilde{\boldsymbol{\omega}} \tag{7}$$

Therefore, based on Equations (5)–(7), we can obtain the following:

$$\dot{\boldsymbol{q}} = \frac{1}{2}\boldsymbol{q} \otimes \tilde{\boldsymbol{\omega}} \tag{8}$$

Substituting Formula (8) into Formula (5), we can obtain

$$\dot{\boldsymbol{q}}^{-1} = -\frac{1}{2}\tilde{\boldsymbol{\omega}} \otimes \boldsymbol{q}^{-1} = -\frac{1}{2}\boldsymbol{\Psi}(\tilde{\boldsymbol{\omega}})\boldsymbol{q}^{-1} \tag{9}$$

The attitudes of the primary spacecraft and secondary spacecraft in the reference frame are represented by quaternions $\boldsymbol{q}_i$ and $\boldsymbol{q}_j$, respectively. The relative attitude $\boldsymbol{q}_{ij}$ in the reference frame is then represented by the following quaternion:

$$\boldsymbol{q}_{ij} = \boldsymbol{q}_i \otimes \boldsymbol{q}_j^{-1} \tag{10}$$

Differentiating Equation (10) gives

$$\dot{\boldsymbol{q}}_{ij} = \dot{\boldsymbol{q}}_i \otimes \boldsymbol{q}_j^{-1} + \boldsymbol{q}_i \otimes \dot{\boldsymbol{q}}_j^{-1} \tag{11}$$

From Equation (7), we can obtain

$$\begin{aligned}
\dot{\boldsymbol{q}}_{ij} &= \frac{1}{2}\bar{\boldsymbol{\Psi}}(\tilde{\boldsymbol{\omega}}_i)\boldsymbol{q}_{ij} - \frac{1}{2}\boldsymbol{q}_i \otimes \tilde{\boldsymbol{\omega}}_j \otimes \boldsymbol{q}_j^{-1} \\
&= \frac{1}{2}\bar{\boldsymbol{\Psi}}(\tilde{\boldsymbol{\omega}}_i)\boldsymbol{q}_{ij} - \frac{1}{2}\bar{\boldsymbol{\Psi}}(\tilde{\boldsymbol{\omega}}_j)\boldsymbol{q}_{ij} \\
&= \frac{1}{2}\overline{\boldsymbol{\Psi}}(\tilde{\boldsymbol{\omega}}_i - \tilde{\boldsymbol{\omega}}_j)\boldsymbol{q}_{ij} \\
&= \frac{1}{2}\overline{\boldsymbol{\Psi}}(\tilde{\boldsymbol{\omega}}_{ij})\boldsymbol{q}_{ij}
\end{aligned} \tag{12}$$

Equation (12) represents the relative attitude motion equation of the primary and secondary spacecraft in the reference frame. It can be observed that the attitude change in the spacecraft is determined by the rotation axis and the rotation angle at each moment. If there is a certain relationship between the laser alignment angle and the rotation angle, it can be constrained to ensure that the spacecraft's attitude change remains within an acceptable range. This issue will be analyzed further below.

#### 2.2.2. Spacecraft Attitude Constraint

From the spacecraft's relative attitude motion equation above, it can be concluded that the spacecraft's attitude during the maneuver process is related to the rotation axis and the rotation angle. Therefore, establishing the relationship between the spacecraft's rotation angle and the laser interferometer arm alignment angle and imposing constraints on this relationship is crucial for ensuring the pointing stability of the laser link during the identification process. The following is a further analysis of this issue.

In gravitational wave detection spacecraft, the optical platform is rigidly connected to the spacecraft. While establishing inter-spacecraft links with distant spacecraft, the optical platform onboard the local spacecraft transmits optical information through optical fibers, thereby constructing a local reference interferometric optical path. As shown in Figure 2, the light red line segments represent the signal beams from the distant spacecraft, the dark red lines represent the local reference beams, and the blue lines represent the test mass reference beams.

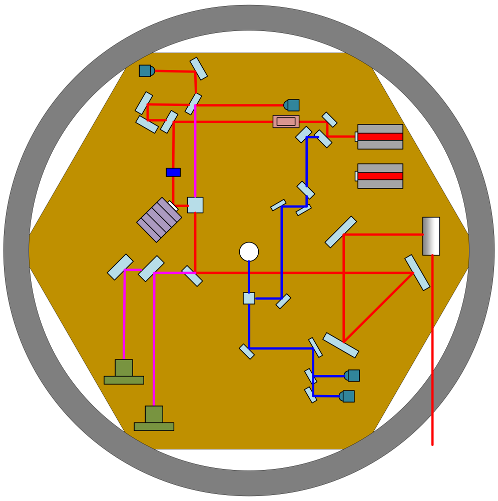

**Figure 2.** Interferometric optical path diagram.

The pointing stability of the laser link is determined by the spacecraft's attitude. As shown in Figure 3, the laser link emitted by the spacecraft is considered a ray segment in space. According to the technical specifications defined in the space gravitational wave detection plan, the allowable alignment error between the laser interferometer arms is 10 nrad. This creates an angular constraint domain, which forms a conical region in space, as shown in Figure 4. Restricting the angle between the two laser interferometer arms within this constraint domain ensures that the gravitational wave detection mission will not be affected.

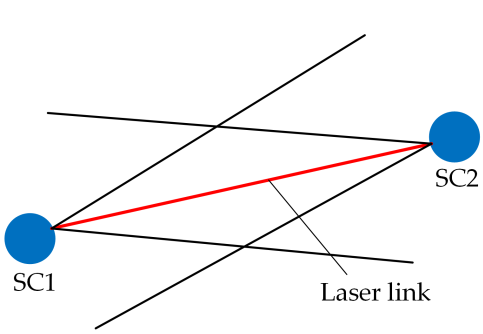


**Figure 3.** Laser alignment diagram.

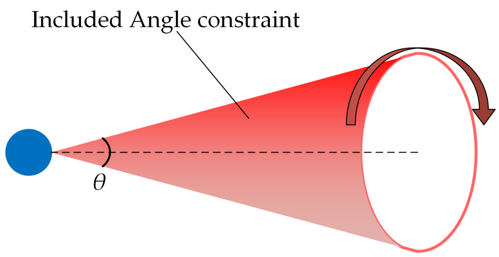


**Figure 4.** Laser angle constraint range diagram.

A mathematical description of the rotational domain formed by the two lasers is provided as follows:

$$\boldsymbol{x}^{\mathrm{T}}\boldsymbol{y}' \geq \cos(\theta_{\max}) \tag{13}$$

In the equation, $\theta_{\max}$ represents the maximum allowable angle for laser alignment in the gravitational wave detection mission. $\boldsymbol{x}$ is the unit vector describing the laser pointing from the primary spacecraft to the secondary spacecraft in the inertial frame. $\boldsymbol{y}$ represents the unit vector of the laser pointing from the secondary spacecraft to the primary spacecraft in the body frame of the secondary spacecraft. $\boldsymbol{y}'$ represents the unit vector of the laser in the inertial frame. The transformation relationship is given by

$$\boldsymbol{y}' = \boldsymbol{y}^2 - 2(\boldsymbol{q}_{ij}^{\mathrm{T}}\boldsymbol{q}_{ij})\boldsymbol{y}^2 + 2(\boldsymbol{q}_{ij}^{\mathrm{T}}\boldsymbol{y}^2)\boldsymbol{q}_{ij} + 2\boldsymbol{q}_0(\boldsymbol{y}^{\times}\boldsymbol{q}_{ij}) \tag{14}$$

Based on Equations (13) and (14), after the calculation, we obtain

$$\boldsymbol{q}_{ij}^{\mathrm{T}}\boldsymbol{M}_2\boldsymbol{q}_{ij} \geq 0 \tag{15}$$

where $\boldsymbol{M}_2 = \begin{bmatrix} d_2 & \boldsymbol{b}_2^{\mathrm{T}} \\ \boldsymbol{b}_2 & A_2 \end{bmatrix}$, $d_2 = \boldsymbol{x}_2^{\mathrm{T}}\boldsymbol{y}_2 - \cos\theta_{\max}$, $\boldsymbol{b}_2 = \boldsymbol{y}_2^{\times}\boldsymbol{x}_2$, and $A_2 = \boldsymbol{x}_2\boldsymbol{y}_2^{\mathrm{T}} + \boldsymbol{y}_2\boldsymbol{x}_2^{\mathrm{T}} - (\boldsymbol{x}_2^{\mathrm{T}}\boldsymbol{y}_2 + 1)\boldsymbol{I}_3$.

This imposes a constraint on the attitude parameters of the spacecraft during the maneuver process, ensuring that the pointing stability of the laser link is maintained during the identification process.

Spacecraft attitude maneuvers are typically achieved using the spacecraft's thrusters. Different attitude changes require applying different excitation signals to the thrusters. Therefore, after completing the analysis of the spacecraft's attitude constraints, the next step is to consider how to apply excitation to the thrusters in order to achieve the required maneuvers that meet the attitude specifications. This issue will be analyzed further below.

### 2.2.3. Spacecraft Maneuver Scheme

This section builds upon Section 2.2.2 and investigates the maneuvering scheme for the spacecraft. The spacecraft's maneuvering during the identification process primarily relies on the activation of the micro-thrusters to generate torque. The generated torque not only drives the spacecraft but also compensates for the effects of perturbative forces. In the case of a gravitational wave detection spacecraft, the thrust provided by the thrusters is determined by the excitation signals applied to the spacecraft. To explore which excitation signals can meet the required attitude states in this study, we investigated the sine wave, cosine wave, and square wave signals. The signal expressions and waveforms are as follows:

$$u = 100sin(2\frac{\pi}{16}t)$$

$$u = 100cos(2\frac{\pi}{16}t)$$

$$u = \begin{cases} 100 & -\frac{T}{2} \leq t \leq 0 \\ -100 & 0 \leq t \leq \frac{T}{2} \end{cases}$$

After applying the three aforementioned excitation signals to the thrusters, it was found that only under cosine wave excitation did the spacecraft's attitude pointing achieve the expected results. The other two excitation signals led to the instability of the spacecraft's attitude. This outcome is related to the specific distribution of thrusters on the spacecraft. Under the gravitational wave detection spacecraft's particular thruster configuration and perturbative force distribution, the application of a cosine wave excitation signal maintains dynamic force balance in all directions, thus achieving the required attitude pointing. Therefore, this paper proposes using a cosine wave signal to drive the thrusters, enabling the stepwise activation of each thruster. Figure 5 and Table 1 show this.

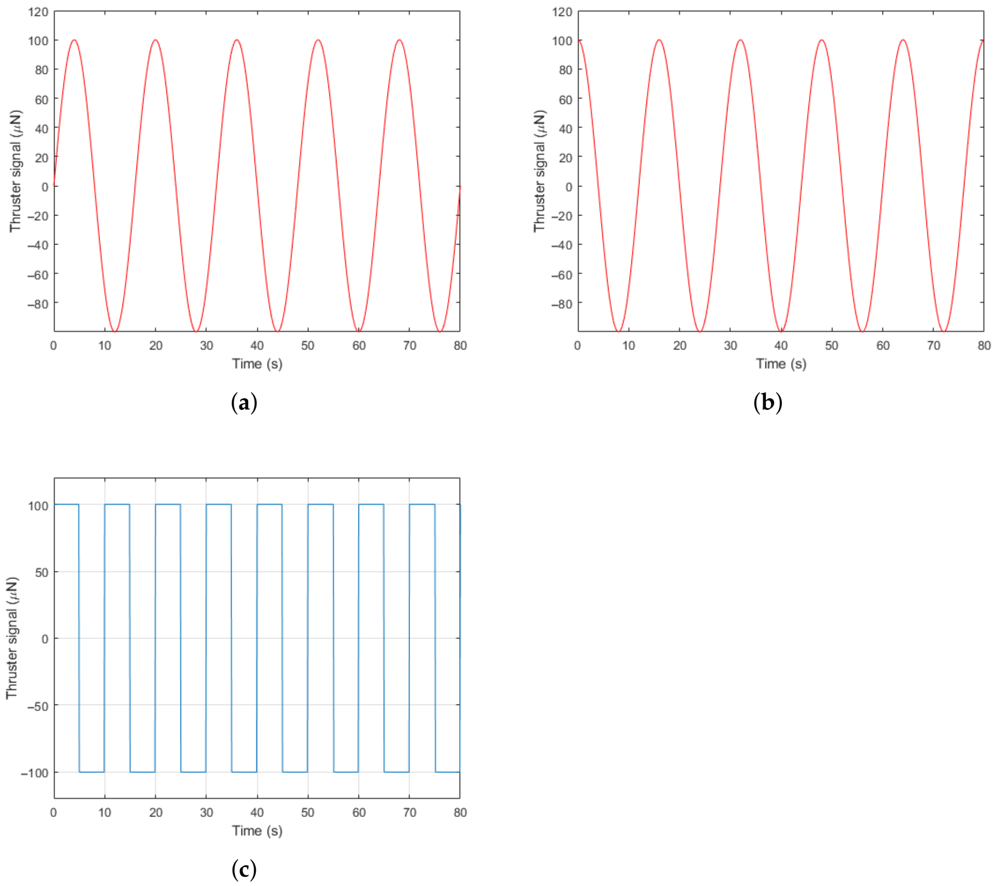


**Figure 5.** Excitation signal: (**a**) sine wave signal; (**b**) cosine wave signal; (**c**) square wave signal.

**Table 1.** The range of the maximum maneuver angle of the spacecraft under three waveforms.

| Signal Type | Maximum Maneuver Angle/Nrad |
|---|---|
| Cosine Wave | $0 \leq \theta \leq 5$ |
| Sine Wave | $\theta \geq 15$ |
| Square Wave | $\theta \geq 500$ |

To ensure that the laser pointing vector remains within the rotational domain during the maneuver, it is also necessary to control the spacecraft's rotation. Let $\boldsymbol{Q}_k = [q_1, q_2, q_3, q_4]$ represent the attitude quaternion of the spacecraft at time k relative to its initial position. Then, we have

$$
\begin{aligned}
Q_k &= Q_1 \otimes Q_2 \otimes \cdots \otimes Q_{k-1} \\
&= \begin{bmatrix} \cos\frac{\Delta\theta}{2} \\ \\ \frac{\Delta\boldsymbol{\theta}}{\Delta\theta}\sin\frac{\Delta\theta}{2} \end{bmatrix}
\end{aligned} \tag{16}
$$

Through solving Equation (16), the angular increment $\Delta\boldsymbol{\theta}$ can be obtained, which represents the spacecraft's rotation angle at time k relative to its initial position. In this paper, a model predictive control (MPC) algorithm was used to predict $\Delta\boldsymbol{\theta}$ to ensure that the spacecraft remains within the rotational domain during the maneuver. The control flow diagram is shown in Figure 6.

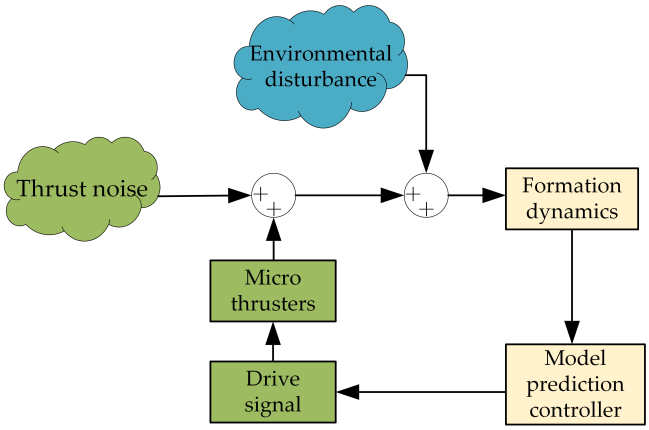


**Figure 6.** Control flow diagram.

Through the above analysis, the study on ensuring the pointing stability of the laser link during the identification process has been completed. The next step is to investigate the center of mass identification algorithm.

## 3. Spacecraft Center of Mass Identification Algorithm Based on Dual-Model Data Fusion

In this study, a dual-model data fusion identification algorithm is proposed that combines the results of the spacecraft dynamics model and the accelerometer measurement model to obtain accurate results. Therefore, it is necessary to separately establish the spacecraft dynamics model and the accelerometer measurement model. Below, we construct the spacecraft dynamics model. Most of the existing literature on spacecraft dynamics models are based on Euler's equations. Hence, in this paper, based on Euler's equations and considering the relative motion of the two spacecraft in the gravitational wave detection mission, we establish the relative motion dynamics model for the two spacecraft in the gravitational wave detection constellation, i.e., the spacecraft formation dynamics model.

In the body frame of the primary spacecraft, the attitude dynamics equation for the primary spacecraft is given by

$$
\boldsymbol{J}_i\dot{\boldsymbol{\omega}}_{bi} + \boldsymbol{\omega}_{bi}^{\times}\boldsymbol{J}_i\boldsymbol{\omega}_{bi} = \boldsymbol{\tau}_{bi} \tag{17}
$$

Similarly, in the body frame of the secondary spacecraft, the attitude dynamics equation for the secondary spacecraft is given by

$$
\boldsymbol{J}_j\dot{\boldsymbol{\omega}}_{bj} + \boldsymbol{\omega}_{bj}^{\times}\boldsymbol{J}_j\boldsymbol{\omega}_{bj} = \boldsymbol{\tau}_{bj} \tag{18}
$$

The relative angular velocity between the spacecraft is expressed in the body frame of the primary spacecraft as

$$\boldsymbol{\omega}_{ij} = \boldsymbol{\omega}_{bi} - \boldsymbol{C}_{ji}\boldsymbol{\omega}_{bj} \tag{19}$$

In Equation (19),

$$\begin{aligned} \boldsymbol{C}_{ji} &= \boldsymbol{C}(\boldsymbol{q}_{ij}) \\ &= \left[ \left( q_{4,ij}^2 - \overline{\boldsymbol{q}}_{ij}^{\mathrm{T}}\overline{\boldsymbol{q}}_{ij} \right) \boldsymbol{I}_3 + 2\overline{\boldsymbol{q}}_{ij}\overline{\boldsymbol{q}}_{ij}^{\mathrm{T}} - 2q_{4,ij}\overline{\boldsymbol{q}}_{ij}^{\times} \right] \end{aligned} \tag{20}$$

Therefore, based on Equations (17) and (18), by differentiating Equation (19), we obtain

$$\begin{aligned} \dot{\boldsymbol{\omega}}_{ij} &= \dot{\boldsymbol{\omega}}_{bi} - \boldsymbol{C}_{ji}\dot{\boldsymbol{\omega}}_{bj} - \dot{\boldsymbol{C}}_{ji}\boldsymbol{\omega}_{bj} \\ &= -\boldsymbol{J}_i^{-1}\boldsymbol{\omega}_{bi}^{\times}\boldsymbol{J}_i\boldsymbol{\omega}_{bi} - \boldsymbol{C}_{ji}\dot{\boldsymbol{\omega}}_{bj} \\ &- \dot{\boldsymbol{C}}_{ji}\boldsymbol{\omega}_{bj} + \boldsymbol{J}_i^{-1}\boldsymbol{\tau}_{bi} \\ &= -\boldsymbol{J}_i^{-1}(\boldsymbol{\omega}_{ij} + \boldsymbol{C}_{ji}\boldsymbol{\omega}_{bj})^{\times}\boldsymbol{J}_i(\boldsymbol{\omega}_{ji} + \boldsymbol{C}_{ji}\boldsymbol{\omega}_{bj}) \\ &- \boldsymbol{C}_{ji}\dot{\boldsymbol{\omega}}_{bj} - \dot{\boldsymbol{C}}_{ji}\boldsymbol{\omega}_{bj} + \boldsymbol{J}_i^{-1}\boldsymbol{\tau}_{bi} \\ &= -\boldsymbol{J}_i^{-1}(\boldsymbol{\omega}_{ij} + \boldsymbol{C}_{ji}\boldsymbol{\omega}_{bj})^{\times}\boldsymbol{J}_i(\boldsymbol{\omega}_{ji} + \boldsymbol{C}_{ji}\boldsymbol{\omega}_{bj}) \\ &- \boldsymbol{C}_{ji}\dot{\boldsymbol{\omega}}_{bj} - \boldsymbol{\omega}_{ij}^{\times}\boldsymbol{C}_{ji}\boldsymbol{\omega}_{bj} + \boldsymbol{J}_i^{-1}\boldsymbol{\tau}_{bi} \end{aligned} \tag{21}$$

In simplifying Equation (19), the relative attitude motion dynamics equation between the primary and secondary spacecraft is obtained as

$$\boldsymbol{J}_i\dot{\boldsymbol{\omega}}_{ij} = -(\boldsymbol{\omega}_{ij} + \boldsymbol{C}_{ji}\boldsymbol{\omega}_{bj})^{\times}\boldsymbol{J}_i(\boldsymbol{\omega}_{ij} + \boldsymbol{C}_{ji}\boldsymbol{\omega}_{bj}) - \boldsymbol{J}_i(\boldsymbol{C}_{ji}\dot{\boldsymbol{\omega}}_{bj} - \boldsymbol{\omega}_{ij}^{\times}\boldsymbol{C}_{ji}\boldsymbol{\omega}_{bj}) + \boldsymbol{\tau}_{bi} \tag{22}$$

In Equation (22), $\boldsymbol{\tau}$ is the driving torque provided by the micro-Niu thruster onboard the gravitational wave detection spacecraft, which can be written as follows:

$$\boldsymbol{\tau}_{bi} = \boldsymbol{F}_{bi} \times (\boldsymbol{r}_{bi} - \Delta\boldsymbol{r}) \tag{23}$$

In the formula, the driving force provided by $\boldsymbol{F}_{bi}$ for the micro-Niu class thruster $\boldsymbol{r}_{bi}$ is the expression of the vector from the point of operation of the thruster to the nominal position of the main spacecraft mass center in the main spacecraft body coordinate system, and $\Delta\boldsymbol{r}$ is the expression of the vector from the actual position to the initial nominal position of the main spacecraft mass center in the main spacecraft body coordinate system, that is, the center of mass offset.

In Equation (23), $\boldsymbol{F}_{bi}$ represents the driving force provided by the micro-Newton thrusters, and $\boldsymbol{r}_{bi}$ is the vector representing the location of the thruster's point of action relative to the nominal position of the primary spacecraft's center of mass, expressed in the primary spacecraft's body frame. $\boldsymbol{d}$ denotes the vector representing the displacement of the primary spacecraft's center of mass from its actual position to the initial nominal position, also expressed in the primary spacecraft's body frame, i.e., the center of mass offset.

Equation (21) is further simplified based on the three properties of the skew-symmetric matrix:

$$\begin{aligned} &\boldsymbol{\zeta}^{\times}\boldsymbol{M} = -\boldsymbol{M}^{\mathrm{T}}\boldsymbol{\zeta}^{\times} \\ &\zeta_1^{\times}\zeta_2 = -\zeta_2^{\times}\zeta_1 \\ &\zeta_1^{\times}\zeta_1 = 0 \end{aligned} \tag{24}$$

$$
\begin{aligned}
\dot{\boldsymbol{\omega}}_{ij} = &-\boldsymbol{J}_i^{-1}\boldsymbol{\omega}_{ij}^{\times}\boldsymbol{J}_i\boldsymbol{\omega}_{ij} - \boldsymbol{J}_i^{-1}\left(\boldsymbol{C}_{ji}\boldsymbol{\omega}_{bj}\right)^{\times}\boldsymbol{J}_i\boldsymbol{\omega}_{bj} \\
&+ \boldsymbol{J}_i^{-1}\left(\boldsymbol{J}_i\boldsymbol{C}_{ji}\boldsymbol{\omega}_{bj}\right)^{\times}\boldsymbol{\omega}_{ij} - (\boldsymbol{C}_{ji}\boldsymbol{\omega}_{bj})^{\times}\boldsymbol{\omega}_{ij} \\
&- \boldsymbol{C}_{ji}\dot{\boldsymbol{\omega}}_{bj} + \boldsymbol{J}_i^{-1}\boldsymbol{\tau}_{bj}
\end{aligned} \tag{25}
$$

Based on Equation (20), the fifth term on the right-hand side of Equation (25) is

$$
\begin{aligned}
\boldsymbol{C}_{ji}\dot{\boldsymbol{\omega}}_{bj} &= \boldsymbol{C}(\boldsymbol{q}_{ij})\dot{\boldsymbol{\omega}}_{bj} \\
&= \left[(q_{4,ij}^2 - \overline{\boldsymbol{q}}_{ij}^{\mathrm{T}}\overline{\boldsymbol{q}}_{ij})\boldsymbol{I}_3 + 2\overline{\boldsymbol{q}}_{ij}\overline{\boldsymbol{q}}_{ij}^{\mathrm{T}} - 2q_{4,ij}\overline{\boldsymbol{q}}_{ij}^{\times}\right]\dot{\boldsymbol{\omega}}_{bj}
\end{aligned} \tag{26}
$$

By simplifying Equation (26), we obtain

$$
\boldsymbol{C}_{ji}\dot{\boldsymbol{\omega}}_{bj} = \boldsymbol{A}_{21}\boldsymbol{q}_{ij} \tag{27}
$$

$$
\mathrm{A}_{21} = \begin{bmatrix}
q_{1,ij}\dot{\omega}_{1,bj} + 2q_{3,ij}\dot{\omega}_{3,bj} & -q_{2,ij}\dot{\omega}_{1,bj} + 2q_{1,ij}\dot{\omega}_{2,bj} & -q_{3,ij}\dot{\omega}_{1,bj} + 2q_{4,ij}\dot{\omega}_{2,bj} & q_{4,ij}\dot{\omega}_{1,bj} - 2q_{2,ij}\dot{\omega}_{3,bj} \\
-q_{1,ij}\dot{\omega}_{2,bj} + 2q_{4,ij}\dot{\omega}_{3,bj} & q_{2,ij}\dot{\omega}_{2,bj} + 2q_{1,ij}\dot{\omega}_{1,bj} & -q_{3,ij}\dot{\omega}_{2,bj} + 2q_{2,ij}\dot{\omega}_{3,bj} & q_{4,ij}\dot{\omega}_{2,bj} - 2q_{3,ij}\dot{\omega}_{1,bj} \\
-q_{1,ij}\dot{\omega}_{3,bj} + 2q_{3,ij}\dot{\omega}_{1,bj} & -q_{2,ij}\dot{\omega}_{3,bj} + 2q_{4,ij}\dot{\omega}_{1,bj} & q_{3,ij}\dot{\omega}_{3,bj} + 2q_{2,ij}\dot{\omega}_{2,bj} & q_{4,ij}\dot{\omega}_{3,bj} - 2q_{1,ij}\dot{\omega}_{2,bj}
\end{bmatrix} \tag{28}
$$

Additionally, we define the following:

$$
\begin{aligned}
\boldsymbol{A}_{22} = &-\boldsymbol{J}_i^{-1}\boldsymbol{\omega}_{ij}^{\times}\boldsymbol{J}_i - \boldsymbol{J}_i^{-1}(\boldsymbol{C}_{ji}\boldsymbol{\omega}_{bj})^{\times}\boldsymbol{J}_i \\
&+ \boldsymbol{J}_i^{-1}(\boldsymbol{J}_i\boldsymbol{C}_{ji}\boldsymbol{\omega}_{bj})^{\times} - (\boldsymbol{C}_{ji}\boldsymbol{\omega}_{bj})^{\times}
\end{aligned} \tag{29}
$$

The simplified form of the relative motion dynamics model can be obtained from the above equations as

$$
\dot{\boldsymbol{\omega}}_{ij} = \boldsymbol{A}_{21}\boldsymbol{\omega}_{ij} + \boldsymbol{A}_{22}\boldsymbol{\omega}_{ij} + \boldsymbol{J}_i^{-1}\boldsymbol{\tau}_{bj} \tag{30}
$$

After establishing the dynamics model, the accelerometer measurement model is developed. The accelerometer measurement output model for the gravitational wave detection spacecraft describes the relative acceleration between the test mass and the electrode cage. The measurement model is given by

$$
\boldsymbol{a}_{out} = \ddot{\boldsymbol{l}} + \dot{\boldsymbol{\omega}} \times \boldsymbol{l} + 2\boldsymbol{\omega} \times \dot{\boldsymbol{l}} + \boldsymbol{\omega} \times (\boldsymbol{\omega} \times l) + \boldsymbol{a}_g + \boldsymbol{a}_n \tag{31}
$$

In the equation, $\boldsymbol{a}_{out}$ represents the theoretical measurement value of the accelerometer. $\dot{\boldsymbol{l}}$ and $\ddot{\boldsymbol{l}}$ represent the first and second derivatives of $\boldsymbol{l}$ with respect to time, respectively. $\boldsymbol{\omega}$ and $\dot{\boldsymbol{\omega}}$ represent the angular velocity and angular acceleration, respectively. $\boldsymbol{a}_g$ is the acceleration caused by the gravitational gradient. The accelerometer measurement model ignores factors such as solid Earth tides, ocean tides, rotational deformations, planetary forces, including those from the Sun and the Moon, and perturbations due to general relativity, as the calibration time is short enough to neglect these effects. Additionally, $\boldsymbol{a}_n$ represents non-gravitational accelerations on the spacecraft, such as atmospheric drag, solar radiation pressure, and Earth's radiation pressure

During the offset calibration period, the center of mass offset of the test mass can be approximated as a constant offset over a short period of time. The first and second partial derivatives in the equation are zero, and therefore, $\boldsymbol{a}_{out}$ can be expressed as

$$
\boldsymbol{a}_{out} = \dot{\boldsymbol{\omega}} \times \boldsymbol{l} + \boldsymbol{\omega} \times (\boldsymbol{\omega} \times \boldsymbol{l}) + \boldsymbol{a}_g + \boldsymbol{a}_n \tag{32}
$$

In assuming the neglect of proportional factors, mismatch errors, and accelerations caused by the gravitational gradient, after substituting the angular velocity and angular acceleration into Equation (31), the accelerometer measurement model can be expressed as

$$\boldsymbol{a}_{out} = \boldsymbol{A}\boldsymbol{l} + \boldsymbol{A}_p + \boldsymbol{A}_e \tag{33}$$

In Equation (33), A can be expressed as

$$\begin{bmatrix} \omega_y^2 + \omega_z^2 & \dot{\omega}_z - \omega_x\omega_y & -\left(\omega_x\omega_z + \dot{\omega}_y\right) \\ \left(\omega_x\omega_y + \dot{\omega}_z\right) & \omega_x^2 + \omega_z^2 & \dot{\omega}_x - \omega_y\omega_z \\ \dot{\omega}_y - \omega_x\omega_z & -\left(\omega_z\omega_y + \dot{\omega}_x\right) & \omega_x^2 + \omega_y^2 \end{bmatrix} \tag{34}$$

In Equation (33), $\boldsymbol{A}_e$ denotes the measurement noise, residual noise, and neglected acceleration terms, while $\boldsymbol{A}_p$ refers to the accelerations caused by the gravitational gradient and non-conservative accelerations, including solar radiation pressure. Since the identification time is relatively short, these are approximated as linear values. Substituting them into Equation (31) gives

$$\boldsymbol{a}_{out} = \boldsymbol{A}\boldsymbol{l} + \alpha t + \beta + \boldsymbol{A}_e \tag{35}$$

In Equation (35), $\alpha$ and $\beta$ represent the slope and intercept after the linear processing of the gravitational gradient and non-conservative forces.

To ensure consistency with real-world conditions, this paper investigates two main types of perturbative accelerations that affect the gravitational wave detection spacecraft.

External perturbations are disturbances caused by space environmental factors acting on the gravitational wave detection spacecraft, including solar radiation pressure torque, gravitational perturbations, thermal environment disturbances, and magnetic field disturbances. Among these, solar radiation pressure is the primary factor. The sunlight incident on the spacecraft's surface generates pressure, which in turn introduces non-gravitational disturbances that must be compensated for. Let the solar irradiance be denoted as $\Phi$, and the resulting pressure is given by

$$P = \frac{\Phi}{c} \tag{36}$$

where $c = 299,792,458\,\mathrm{m/s}$ is the speed of light in a vacuum. The solar irradiance is approximately $\Phi \approx 1371\,\mathrm{W/m^2}$, and the corresponding solar radiation pressure is $P = 4.6 \times 10^{-6}\,\mathrm{N/m^2}$. Solar radiation can interact with the spacecraft's surface in four different ways, and the sum of the proportions of these four interactions is equal to 1:

$$C_a{+}C_s{+}C_d{+}C_t{=}1 \tag{37}$$

where $C_a$ is the absorption coefficient, $C_s$ is the specular reflectance, $C_d$ is the diffuse reflectance, and $C_t$ is the transmissivity.

The spacecraft can be simplified as a polyhedral structure. Let $\boldsymbol{A}_k$ denote the area of the $k$-th surface exposed to sunlight, and let $\boldsymbol{n}_k^s$ and $\boldsymbol{s}_k^s$ represent the unit vectors of the normal and the direction opposite to the incident light in the spacecraft's body reference frame, respectively. The non-conservative force due to solar radiation pressure on this surface is

$$\begin{aligned} \boldsymbol{F}_{s,k}^s &= -P\cos\alpha_k \boldsymbol{A}_k (1 - C_{s,k})\boldsymbol{s}_k^s \\ &-2P\cos\alpha_k \boldsymbol{A}_k \left(C_{s,k}\cos\alpha_k + \tfrac{1}{3}C_{d,k}\right)\boldsymbol{n}_k^s \end{aligned} \tag{38}$$

Further, let the coordinates of the centroid of each surface be denoted as $\boldsymbol{r}_{sk}^{s}$. The resultant torque caused by solar radiation pressure is then given by

$$\boldsymbol{F}_s^s = \sum_k \boldsymbol{F}_{s,k}^s \tag{39}$$

$$\boldsymbol{M}_s^s = \sum_k \boldsymbol{r}_k^s \times \boldsymbol{F}_{s,k}^s \tag{40}$$

In addition, the Earth's gravitational field can also interfere with the spacecraft's motion. The Earth's gravitational field is typically described using the gravitational potential, which is the negative of the gravitational potential energy. It can be expressed in spherical harmonic expansion as

$$\begin{gathered} U(r,\theta,\lambda) = -\frac{V(r,\theta,\lambda)}{m} \\ = \frac{\mu}{r}\sum_{n=0}^{\infty}\sum_{m=0}^{n}\frac{R_e^n}{r^n}P_{nm}(\cos\theta)C_{nm}\cos m\lambda + \frac{\mu}{r}\sum_{n=0}^{\infty}\sum_{m=0}^{n}\frac{R_e^n}{r^n}P_{nm}(\cos\theta)S_{nm}\sin m\lambda \end{gathered} \tag{41}$$

In the equation, $V(r,\theta,\lambda)$ is the gravitational potential energy of a point mass $m$, $R_e$ is the Earth's radius, $r$ is the distance between the point mass and the Earth's center of mass, $\theta$ is the co-latitude, and $\lambda$ is the longitude. The term $P_{nm}(\cdot)$ refers to the associated Legendre polynomials, which are derived from the Legendre polynomials $P_n(\cdot)$.

Thus, the spacecraft dynamics model and accelerometer measurement model have been established. However, the results from a single model often contain significant computational errors, and even with the application of filtering algorithms, accurate identification results cannot be obtained. The core issue of the identification algorithm is how to fuse the results from both models to obtain more accurate outcomes. The following section will analyze the identification algorithm proposed in this study.

This study proposes a dual-model data fusion algorithm for spacecraft center of mass identification based on the least squares method. The algorithm separately estimates the center of mass displacement using the established spacecraft dynamics model and accelerometer measurement model and then fuses the results obtained from both models using the least squares method to achieve more accurate outcomes. The flowchart of the proposed algorithm is shown in Figure 7.

First, based on the established spacecraft's relative motion kinematics model, a posture controller is designed to control the spacecraft's maneuvers, ensuring that the spacecraft remains within the rotation domain. Then, the spacecraft's motion data are output to both the accelerometer measurement model and the dynamics model, with disturbances added. The two models are solved separately to obtain initial estimates. Finally, the least squares method is applied to optimize the initial estimates, yielding an accurate center of mass position estimate.

The following is an analysis of the specific process for the spacecraft's center of mass position identification using the dual-model data fusion algorithm.

To further improve the identification accuracy of the algorithm, it is necessary to preprocess the identification results of individual models through filtering. In this study, Kalman filtering was applied to preprocess the identification results of the two models separately.

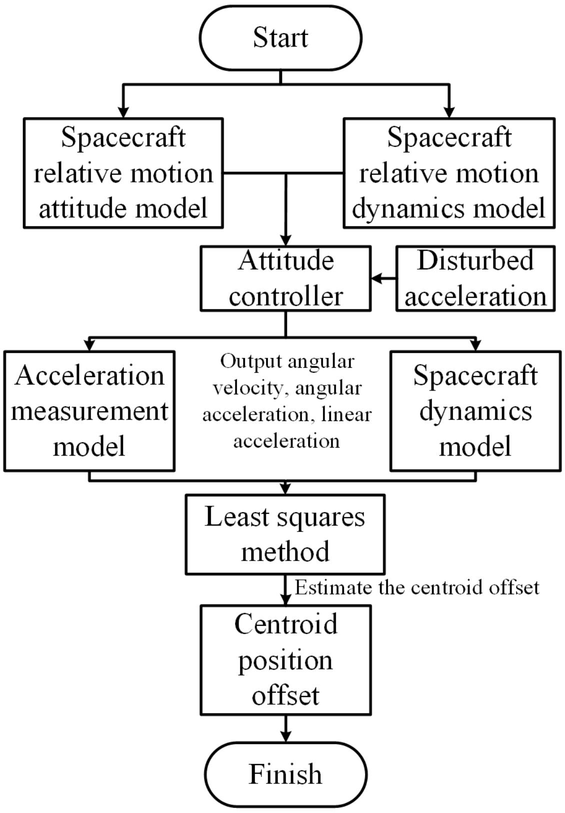


**Figure 7.** Algorithm flow.

The state variable is defined as the mass center, with the true value denoted as $\boldsymbol{X} = [d_x, d_y, d_z]$, and the derivative set to zero. From this, the state equation is derived as

$$\hat{\boldsymbol{X}}_k = \boldsymbol{F}_{k,k-1}\boldsymbol{X}_{k-1} \tag{42}$$

In the equation, $k$ denotes the step number of the Kalman filter, and $\boldsymbol{F}_{k,k-1}$ represents the state transition matrix from step $k$ to step $k-1$.

The observation equation is expressed as

$$\boldsymbol{Z}_{\mathrm{out},k} = \boldsymbol{H}_k\boldsymbol{X}_k + \boldsymbol{v}_k \tag{43}$$

In this equation, $\boldsymbol{H}_k$ represents the measurement matrix, and $\boldsymbol{v}_k$ denotes the measurement noise, which follows a standard normal distribution.

In removing the measurement noise, the prior observation equation is given by

$$\hat{\boldsymbol{Z}}_{\mathrm{out},k} = \boldsymbol{H}_k\hat{\boldsymbol{X}}_k \tag{44}$$

The state estimation error covariance matrix is given by

$$\hat{\boldsymbol{P}}_k = \boldsymbol{F}_{k,k-1}\boldsymbol{P}_{k-1}\boldsymbol{F}_{k,k-1}^{\mathrm{T}} + \boldsymbol{Q}_{k-1} \tag{45}$$

where $\boldsymbol{Q}$ represents the process noise covariance matrix.

The Kalman gain is expressed as

$$\boldsymbol{K}_k = \hat{\boldsymbol{P}}_k\boldsymbol{H}_k^{\mathrm{T}}\left(\boldsymbol{H}_k\hat{\boldsymbol{P}}_k\boldsymbol{H}_k^{\mathrm{T}} + \boldsymbol{R}_k\right)^{-1} \tag{46}$$

where $\boldsymbol{R}$ represents the measurement noise covariance matrix.

From this, the state update equation can be obtained as

$$\boldsymbol{X}_k = \hat{\boldsymbol{X}}_k + \boldsymbol{K}_k\left(\boldsymbol{Z}_{\mathrm{out},k} - \hat{\boldsymbol{Z}}_{\mathrm{out},k}\right) \tag{47}$$

where $\hat{\boldsymbol{X}}_k$ denotes the priori state estimate, and $\boldsymbol{X}_k$ represents the posteriori state estimate.

Meanwhile, the covariance matrix of the state estimation error is given by

$$\boldsymbol{P}_k = (\boldsymbol{I} - \boldsymbol{K}_k\boldsymbol{H}_k)\hat{\boldsymbol{P}}_k(\boldsymbol{I} - \boldsymbol{K}_k\boldsymbol{H}_k)^{\mathrm{T}} + \boldsymbol{K}_k\boldsymbol{R}_k\boldsymbol{K}_k^{\mathrm{T}} \tag{48}$$

Through continuous iterations, the center of mass offset $\boldsymbol{d}$ can be obtained.

After preprocessing the identification results of the individual model, they will be incorporated into the dual-model algorithm.

In the accelerometer model, the estimated value of the center of mass offset is represented as $\boldsymbol{X}_1 = [d_{x1}, d_{y1}, d_{z1}]$, with the derivative set to zero. Simplifying Equation (35) gives

$$\boldsymbol{A}_{rota} = \boldsymbol{a}_{out} - \alpha t - \beta - \boldsymbol{A}_e = \boldsymbol{A}\boldsymbol{X}_1 \tag{49}$$

In Equation (49), $\boldsymbol{A}_{rota}$ represents the acceleration induced by the maneuver, from which the following can be derived:

$$\boldsymbol{X}_1 = \boldsymbol{A}^{-1}\boldsymbol{A}_{rota} \tag{50}$$

The estimated value of the center of mass offset in the dynamic model is denoted as $\boldsymbol{X_1} = [d_x1, d_y1, d_z1]$. By processing Equation (30), we obtain

$$\dot{\boldsymbol{\omega}}_{ij} = \boldsymbol{A}_{21}\boldsymbol{\omega}_{ij} + \boldsymbol{A}_{22}\boldsymbol{\omega}_{ij} + \boldsymbol{J}_i^{-1}\boldsymbol{F}_{bi} \times (\boldsymbol{r}_{bi} - \boldsymbol{X}_2) \tag{51}$$

By processing Equation (51), we obtain

$$\boldsymbol{X}_2 = \boldsymbol{r}_{bi} - (\boldsymbol{J}_i^{-1}\boldsymbol{F}_{bi})^{-1} \times (\dot{\boldsymbol{\omega}}_{ij} - \boldsymbol{A}_{21}\boldsymbol{\omega}_{ij} - \boldsymbol{A}_{22}\boldsymbol{\omega}_{ij}) \tag{52}$$

Next, we define the calculation error as $\boldsymbol{e}_1 = \boldsymbol{X} - \boldsymbol{X}_1$ and $\boldsymbol{e}_2 = \boldsymbol{X} - \boldsymbol{X}_2$. The sum of the squared errors is then given by

$$\boldsymbol{S} = \sum_{i=1}^{n}\left(\frac{(\boldsymbol{X}_i - \boldsymbol{X}_{1i})^{\mathrm{T}}(\boldsymbol{X}_i - \boldsymbol{X}_{1i})}{\boldsymbol{s}_{1i}^{\mathrm{T}}\boldsymbol{s}_{1i}} + \frac{(\boldsymbol{X}_i - \boldsymbol{X}_{2i})^{\mathrm{T}}(\boldsymbol{X}_i - \boldsymbol{X}_{2i})}{\boldsymbol{s}_{2i}^{\mathrm{T}}\boldsymbol{s}_{2i}}\right) \tag{53}$$

In Equation (53), s1 and s2 represent the standard deviations of the results from the two models, and $\boldsymbol{S}$ denotes the loss function.

In taking the derivative with respect to $\boldsymbol{X}$, the least squares solution for $\boldsymbol{X}$ is obtained as

$$\boldsymbol{X}_i = \frac{\boldsymbol{X}_{1i}\boldsymbol{s}_{2i}^{\mathrm{T}}\boldsymbol{s}_{2i} + \boldsymbol{X}_{2i}\boldsymbol{s}_{1i}^{\mathrm{T}}\boldsymbol{s}_{1i}}{\boldsymbol{s}_{1i}^{\mathrm{T}}\boldsymbol{s}_{1i} + \boldsymbol{s}_{2i}^{\mathrm{T}}\boldsymbol{s}_{2i}} \tag{54}$$

In Equation (54), $\boldsymbol{i}$ denotes the result of the $\boldsymbol{i}$-th computation.

After obtaining the model calculation data, due to the influence of noise, the results may contain outliers. Through removing these outliers to smooth the data, the accuracy of the least squares solution can be ensured. The Z-score method is then applied to smooth the results of the two models.

Define $\boldsymbol{C} = [\boldsymbol{X}_{1z}\boldsymbol{X}_{2z}]$, where $\boldsymbol{X}_{1z}$ and $\boldsymbol{X}_{2z}$ represent the concatenated results from the two models. The mean vector of $\boldsymbol{C}$ is given by

$$\boldsymbol{\mu} = \frac{1}{m+n}\sum_{i=1}^{m+n}\boldsymbol{C}_i \quad (55)$$

In Equation (55), $m$ and $n$ represent the number of data points in the results of the two models, respectively.

The covariance matrix of $\boldsymbol{C}$ is

$$\boldsymbol{S} = \frac{1}{m+n-1}\sum_{i=1}^{m+n}(\boldsymbol{C}_i - \boldsymbol{\mu})(\boldsymbol{C}_i - \boldsymbol{\mu})^{\mathrm{T}} \quad (56)$$

For each data point $\boldsymbol{C}_i$, its Mahalanobis distance is calculated as

$$D_M(\boldsymbol{C}_i) = \sqrt{(\boldsymbol{C}_i - \boldsymbol{\mu})^{\mathrm{T}}\boldsymbol{S}^{-1}(\boldsymbol{C}_i - \boldsymbol{\mu})} \quad (57)$$

Next, choose a significance level $\alpha$ and find the corresponding critical value from the chi-square distribution with k degrees of freedom. The squared Mahalanobis distance is then compared with this critical value, and data points exceeding the threshold are considered outliers and removed.

The dual-model data fusion algorithm proposed in this paper is theoretically capable of effectively suppressing the impact of computational and data errors on the results. To validate the effectiveness of the proposed algorithm, a simulation verification is presented below.

## 4. Simulation Verification of Center of Mass Identification Algorithm

### *4.1. Simulation Parameter Setting*

A simulation model was established based on the geometric parameters of a certain type of gravitational wave detection spacecraft. A three-axis estimation error was defined as $d$. The initial laser vector was positioned along the high line of the conical rotation domain, and the spacecraft's inertia tensor was as follows:

$$\boldsymbol{J} = \begin{bmatrix} 1020 & 0 & 0 \\ 0 & 1823 & 0 \\ 0 & 0 & 1018 \end{bmatrix} \mathrm{kg}\cdot\mathrm{m}^2$$

Based on the latest research on the laser link angle of gravitational wave detection spacecraft, the measurement precision of the sensor was set as follows in the simulation experiment: the angular velocity measurement accuracy was $1 \times 10^{-8}$ rad/s, and the angular acceleration measurement accuracy was $1 \times 10^{-6}$ rad/s$^2$. The standard deviations of the model calculation results were set to $10^{-6}$ and $10^{-5}$, respectively [13].

### *4.2. Analysis of Simulation Results*

#### 4.2.1. Effect Analysis of Attitude-Constrained Maneuvering Scheme

Referencing the method for ensuring laser link pointing described in Section 2.2, this study verified the spacecraft's laser link pointing method. Based on the pointing constraint method proposed in this paper, the attitude controller is used to control the spacecraft's rotation, ensuring that the two spacecraft maintain maneuvering within the rotation domain during their relative motion. This guarantees that the laser alignment angle consistently meets the 10 nrad requirement. Additionally, in taking the primary spacecraft as an example, the angular velocity, angular acceleration, and acceleration data of the primary spacecraft were measured. The maneuvering trajectories of the two spacecraft are shown in Figures 8 and 9, with the rotation domain shown in Figure 10. The angle between the laser vector after each rotation and its initial position was measured, and the simulation results are presented in Figure 11.

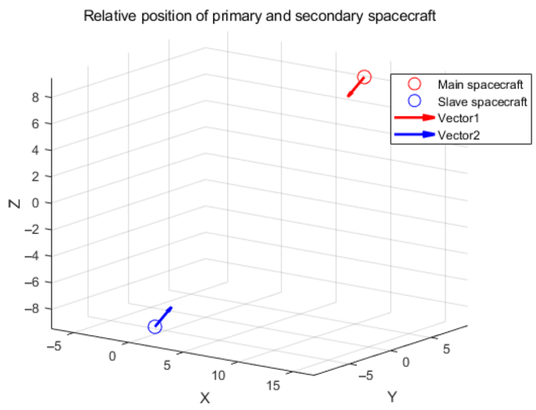


**Figure 8.** The position of the two spacecraft in space.

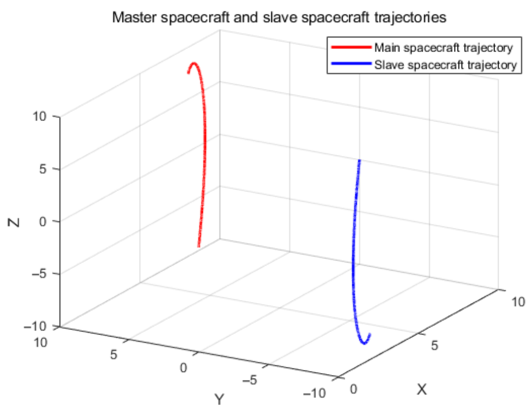


**Figure 9.** Motion trajectories of the two spacecraft.

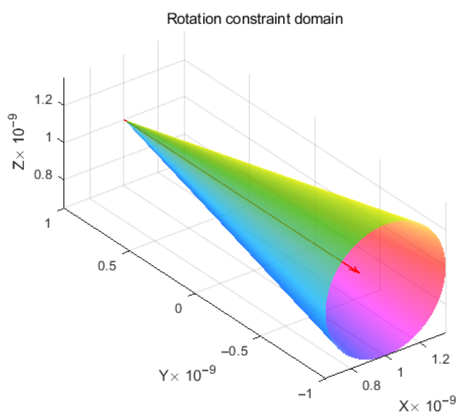


**Figure 10.** The rotational domain of the spacecraft.

From Figures 8 and 9, it can be observed that in using the laser link pointing method proposed in this paper, the trajectories of the primary and secondary spacecraft exhibit a mirror-symmetrical pattern, indirectly confirming that the laser link angle remains within a small range. As shown in Figure 11, during the spacecraft's maneuvering process, the laser link angle consistently stays below 10 nrad, meeting the requirements for the laser link angle in the gravitational wave detection mission. This directly demonstrates the effectiveness of the proposed method.

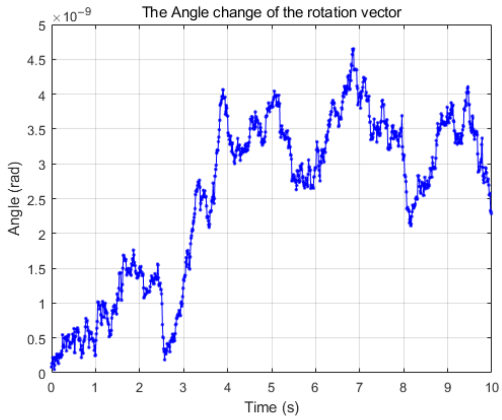


**Figure 11.** Change in laser link angle.

#### 4.2.2. Analysis of Center of Mass Identification Effect

To obtain the accurate identification accuracy of the proposed method, the three-axis center of mass offset was set to 0.2 mm, following the simulation parameters in Section 4.1. During the spacecraft's rotational maneuver, the angular velocity, angular acceleration, and acceleration data of the main spacecraft were collected under the protected laser link pointing method described in Section 2.2. To simulate the impact of space non-conservative forces on the spacecraft's attitude, perturbation force noise was introduced into the simulation. The acceleration noise caused by the perturbation force significantly affects the center of mass identification process. Therefore, the acceleration data were filtered to eliminate the noise caused by the perturbation force. The filtered maneuver data were then substituted into both the accelerometer model and the dynamics model to solve for the initial estimates. These initial estimates were processed using the least squares method described in Section 2, and the resulting three-axis estimation errors are shown in Figure 12. Additionally, a simulation comparison was made for the case without perturbation force removal, with the results shown in the figure.

From Figure 12, it can be observed that, under the premise of ensuring laser link alignment, the identification accuracy of the spacecraft's center of mass offset proposed in this paper can reach the micron level. The average identification accuracy for all three axes is 15 μm. Additionally, some spikes are visible in the range between 0 and 350, which are caused by the introduction of random noise during the identification process. Furthermore, it can be seen that the convergence speed of the curve is relatively fast, with convergence occurring after 240, indicating that the proposed algorithm performs well in terms of response speed.

On the other hand, by applying filtering, this study reduces the impact of non-conservative forces on the center of mass identification accuracy. Figure 12c,d show the identification results considering the effects of solar radiation pressure and the Earth's gravitational field, respectively. From the figures, it can be observed that non-conservative forces have a significant impact on the identification results. Without filtering the acceleration signals, the results diverge, making it impossible to obtain valid center of mass offset data. This indicates that the acceleration accuracy has considerable influence on center of mass identification, highlighting the necessity of considering non-conservative forces, and also validates the reliability of the proposed model.

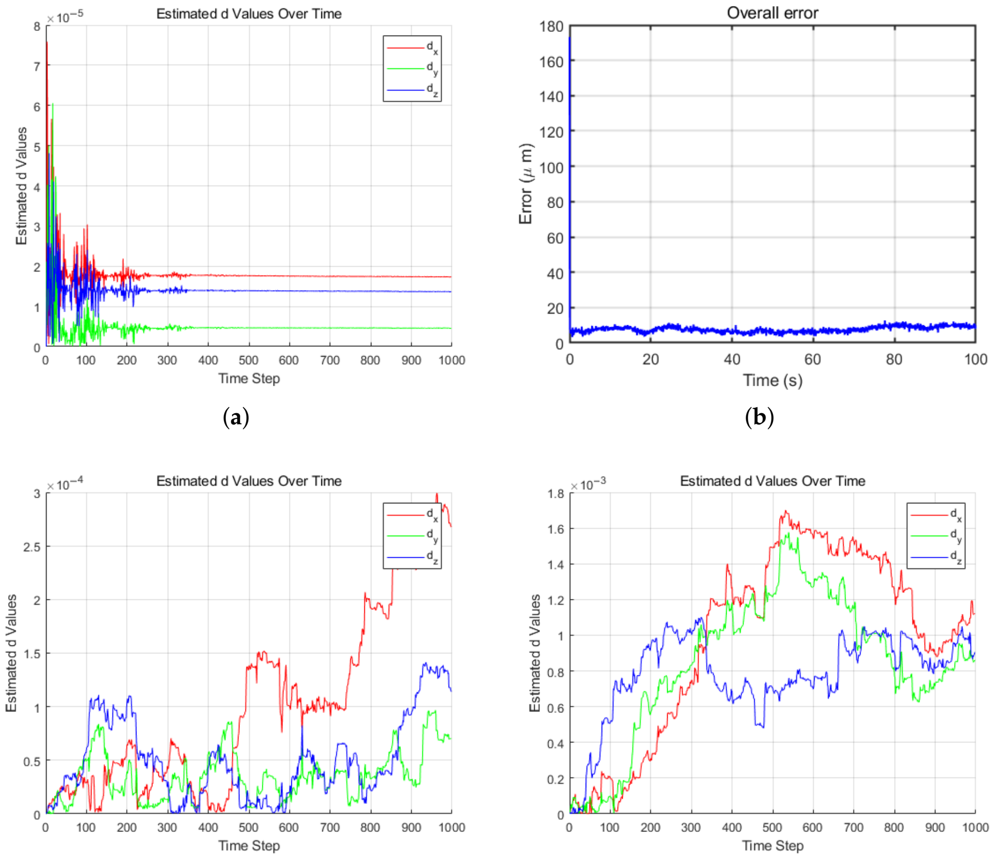


(**a**) (**b**) (**c**) (**d**)

**Figure 12.** Identification results: (**a**) three-axis estimation error; (**b**) overall error; (**c**) estimation error without removing solar radiation pressure; (**d**) estimation error without removing gravitational field effect.

Equally important is that, in the research context of this paper, the thruster plays a crucial role in the attitude of the spacecraft. Therefore, the noise of the thruster will affect the identification results of the center of mass. We carried out simulation verifications for different thruster noise conditions, and the simulation results are presented in Table 2.

**Table 2.** Simulation parameters.

| Type | Data |
|---|---|
| Thrust noise/μN | 0.3 |
| Angular velocity accuracy/rad·s$^{-1}$ | $1 \times 10^{-8}$ |
| Angular acceleration accuracy/rad·s$^{-2}$ | $1 \times 10^{-6}$ |

As can be seen from the results presented in Table 3, the noise generated by the thruster exerts substantial influence on the precision of the identification outcomes. Specifically, with the augmentation of the thruster's noise level, the identification accuracy exhibits a continuous downward trend. Hence, during actual identification procedures, it becomes essential to implement a certain degree of filtering on the thrust noise. Moreover, this further substantiates the validity of the model proposed in this paper, endowing it with the capability to proficiently validate the dynamic responses of the spacecraft under diverse external impacts in real-world scenarios.

**Table 3.** Simulation results under different thrust noise levels.

| Thrust Noise/μN | Identification Accuracy/μm |
|---|---|
| 0.3 | 25 |
| 0.8 | 55 |
| 1.5 | 108 |

Next, the proposed algorithm was verified through simulation. An important step in the proposed dual-model data fusion algorithm is the removal of outliers in the data, which significantly improves the identification accuracy. To compare with the case without outlier removal, a comparative simulation was conducted based on the existing setup.

As shown in Figure 13, the identification accuracy decreased by an order of magnitude when outliers were not removed. This is because the outliers affected the overall data. It is evident that outliers have a significant impact on the identification accuracy. The outlier removal process in the proposed algorithm effectively improves the identification accuracy, thus demonstrating the effectiveness of the proposed algorithm.

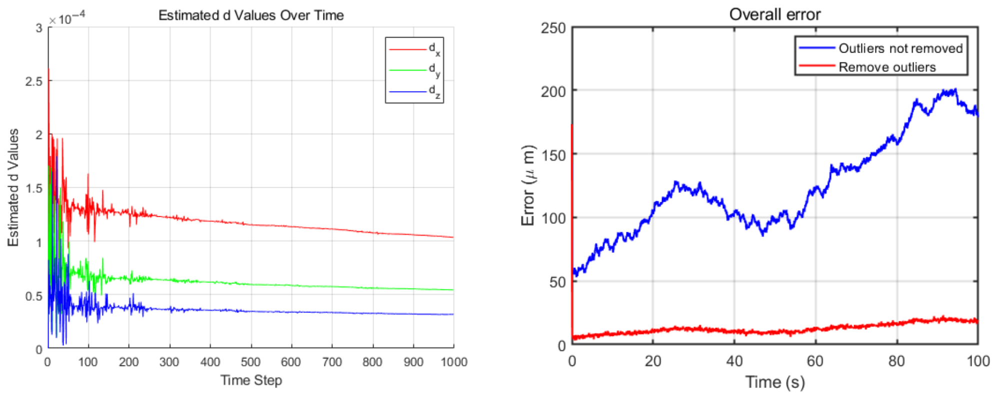


(**a**) (**b**)

**Figure 13.** Error comparison chart with outliers removed: (**a**) three-axis error; (**b**) overall error.

Outlier removal can effectively improve the identification accuracy. However, the main advantage of the proposed algorithm lies in the use of dual-model data fusion. The superiority of the dual-model data fusion algorithm is that it minimizes the identification errors caused by the uncertainties of a single model, leading to significant improvement in the overall identification accuracy. To demonstrate the superiority of this algorithm over single-model calculations, the center of mass offset was estimated using both the accelerometer model and the dynamics model. The identification errors are shown in Figure 14.

As shown in Figure 14, compared to the identification algorithm proposed in this paper, the estimation accuracy using a single model decreased by an order of magnitude. It is also evident that the fluctuations in the initial phase of the single-model identification are much larger. One reason for this is that the noise errors in a single model are difficult to eliminate using only its own data, resulting in large initial identification errors. Another reason is that the method proposed in this paper incorporates the fusion of two data sets and removes outliers from the data, which improves both the response speed and the identification accuracy. Additionally, in the dynamics model estimation results, a spike phenomenon is still observed in the interval between 900 and 1000, which is due to the single model's inability to effectively eliminate the random noise introduced, coupled with the presence of outliers, preventing the estimation results from becoming smooth.

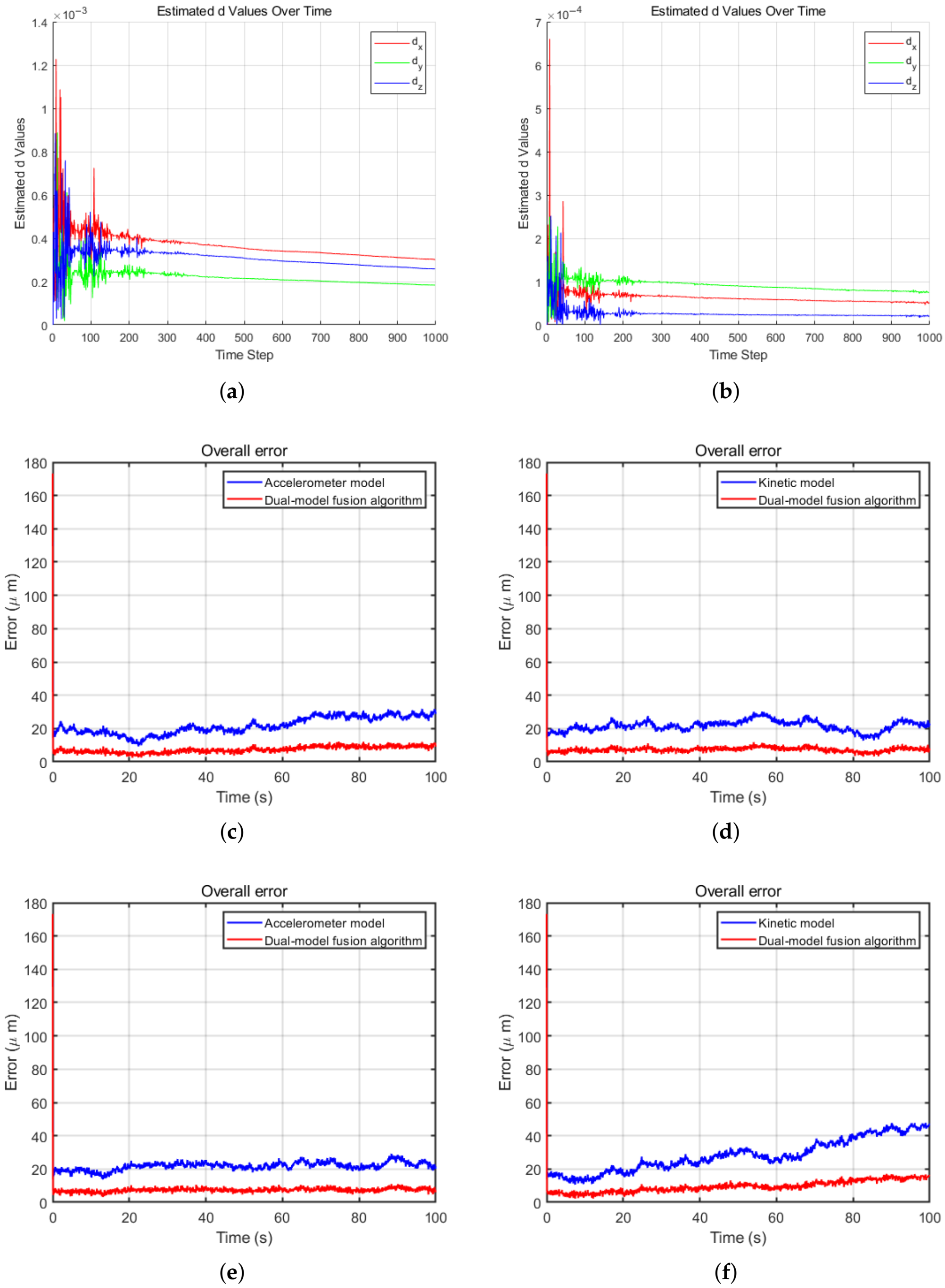


**Figure 14.** Single-model estimation error: (**a**) accelerometer model; (**b**) kinetic model; (**c**) under condition 1, the proposed model and the accelerometer model; (**d**) under condition 1, the proposed model and the dynamics model; (**e**) under condition 2, the proposed model and the accelerometer model; (**f**) under condition 2, the proposed model and the dynamics model.

Then, to verify the universality of the proposed algorithm for center of mass identification, three operating conditions were selected: fully positive three-axis offset, fully negative three-axis offset, and varying three-axis offsets. The identification results are shown in the figure below.

From the simulation results shown in the Figure 15 and Table 4, it can be observed that the proposed algorithm maintains excellent identification accuracy under different center of mass offsets. Whether the three-axis offsets are the same or different, the algorithm consistently demonstrates good performance without significant deviation in accuracy along any particular axis. This further confirms the universality of the proposed algorithm.

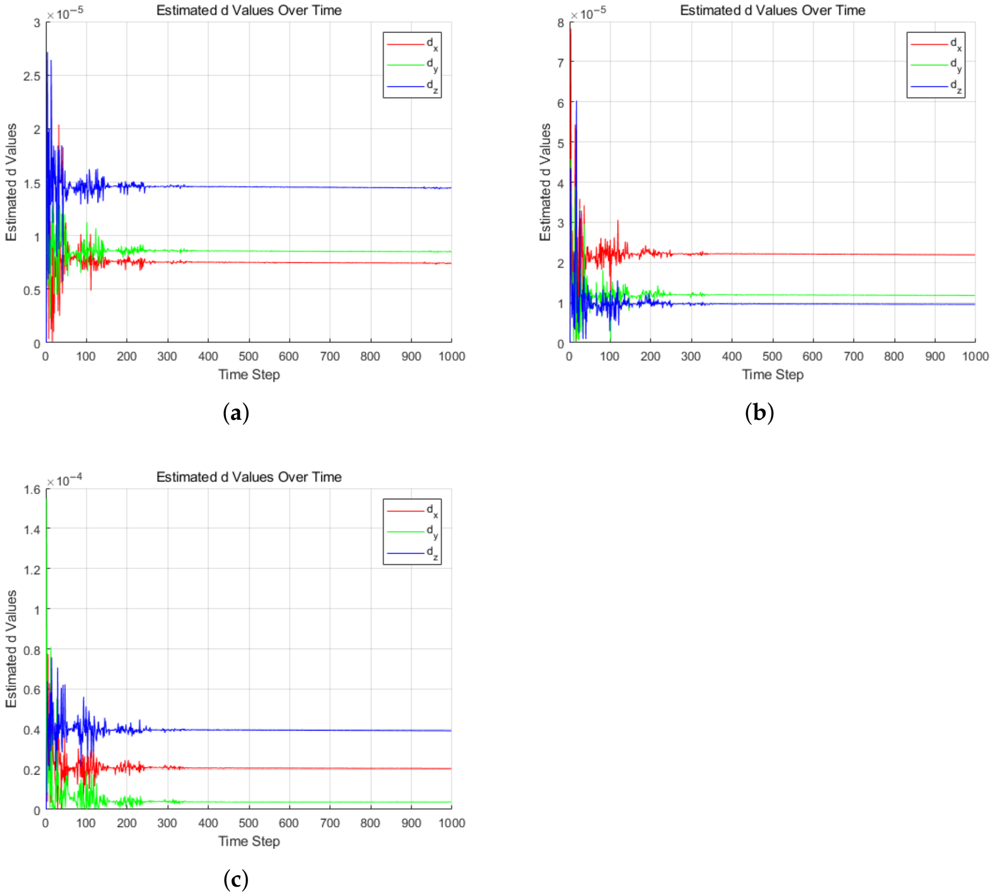


**Figure 15.** Identification results under different center of mass offsets: (**a**) the offset is [−150, −150, −150] µm; (**b**) the offset is [250, 250, 250] µm; (**c**) the offset is [150, 200, 250] µm.

**Table 4.** Identification results under different mass center offsets.

| Center of Mass Offset | Identification Precision |
|---|---|
| $[-150, -150, -150]$ µm | 15 µm |
| $[250, 250, 250]$ µm | 20 µm |
| $[150, 200, 250]$ µm | 40 µm |

The above analysis validates the superiority of the identification algorithm proposed in this paper. On the other hand, to compare the center of mass identification results without considering the laser interferometer's arm alignment, the identification results from two referenced studies are used for comparison. The performance comparison is shown in the following figure.

From the Figure 16 and Table 5, it can be observed that compared to the identification accuracy in "Reference 12", the method proposed in this paper achieves a similar accuracy level. Although there is a difference of 5 µm in the specific accuracy values, "Reference 12" did not consider the alignment of the laser link, so in terms of scientific mission detection accuracy, the method proposed in this paper outperforms "Reference 12".

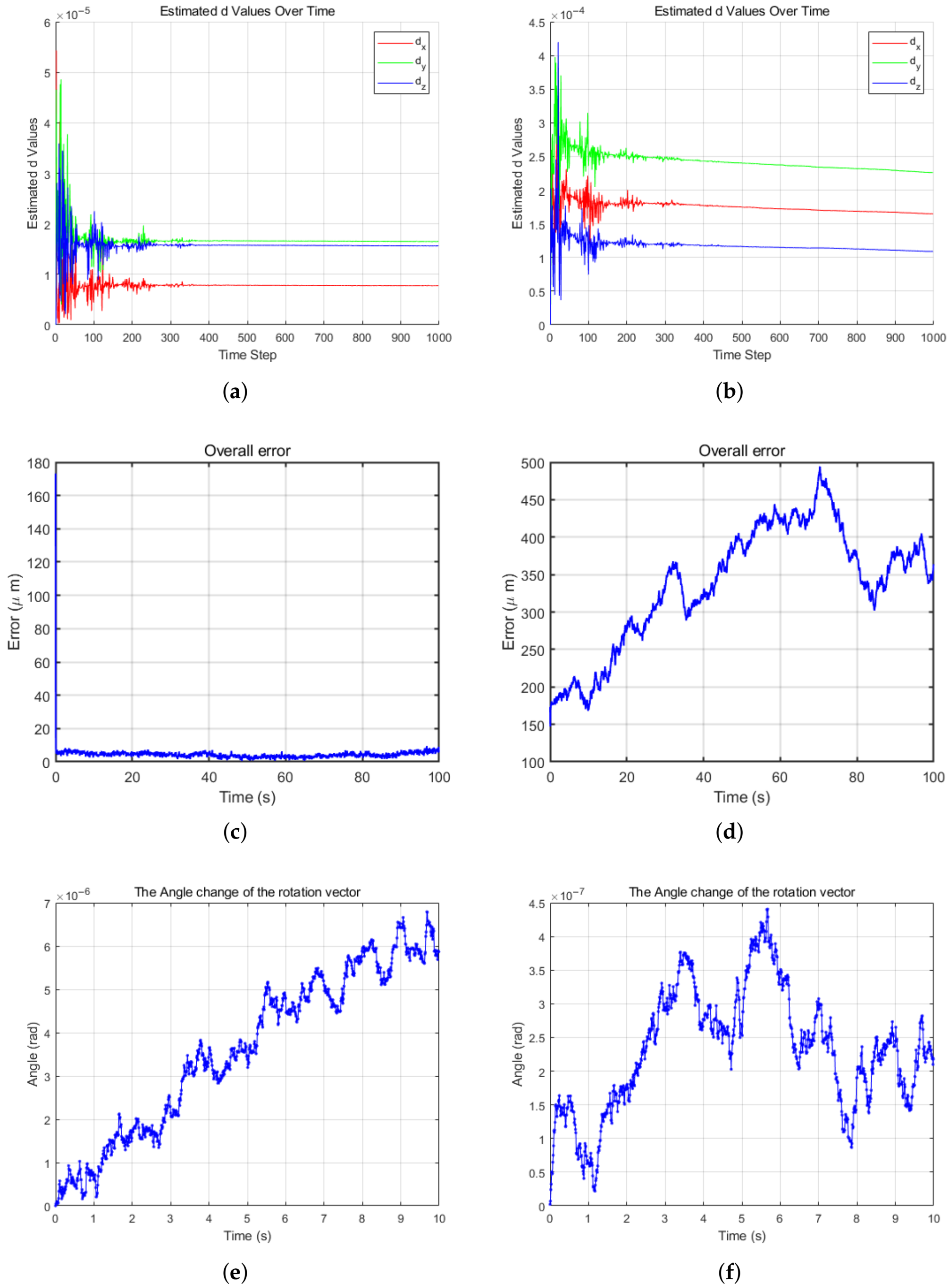


**Figure 16.** Identification results using methods from the literature: (**a**) "Reference 12" estimated error; (**b**) "Reference 13" estimated error; (**c**) "Reference 12" over error; (**d**) "Reference 13" over error; (**e**) laser alignment Angle in "Reference 12"; (**f**) laser alignment Angle in "Reference 13".

"Reference 13" considers center of mass identification while maintaining the laser link pointing accuracy. However, when compared to the results of this study, even though "Reference 13" addresses the laser alignment issue, it does not constrain the laser angle within 10 nrad. Additionally, the identification accuracy in "Reference 13" is three orders of magnitude lower than that with the proposed method. In comparing the center of mass identification results of "References 12 and 13", the effectiveness of the method proposed in this paper in ensuring center of mass identification under laser link alignment is validated.

**Table 5.** Initial nominal orbit parameters of the spacecraft.

| Method | Identification Precision |
|---|---|
| Textual Method | 15 µm |
| Reference 12 Methods | 10 µm |
| Reference 13 Methods | 550 µm |

## 5. Discussion and Conclusions

Through numerical simulations under different operating conditions, it was demonstrated that the proposed algorithm achieves an excellent center of mass offset identification accuracy for gravitational wave detection spacecraft, while ensuring that the laser interferometer arm alignment angle remains within the constrained range throughout the identification process. Compared to other algorithms, the proposed method still achieves good accuracy while considering the laser pointing, highlighting the superiority of the algorithm.

This paper addresses the problem of center of mass position identification for gravitational wave detection spacecraft by establishing a dynamic model that considers the spacecraft's relative motion and attitude. It investigates a spacecraft maneuvering method that ensures the laser link pointing accuracy, enabling the spacecraft to maneuver while maintaining the required laser link alignment. Additionally, a center of mass identification algorithm based on dual-model data fusion is proposed, achieving high-precision center of mass identification with minimal attitude changes in the spacecraft.

Simulation results demonstrate that, under the proposed method, the spacecraft's laser interferometer arm alignment accuracy is consistently maintained within 10 nrad, and the center of mass identification accuracy reaches 15 µm. This represents a significant improvement in precision compared to existing methods and provides a more accurate data foundation for subsequent center of mass adjustment tasks with spacecraft. Furthermore, the proposed method offers valuable insights for center of mass identification in other ultra-stable spacecraft.

In future work, based on this study, further research will be conducted on center of mass adjustment methods suitable for ultra-stable spacecraft.

**Author Contributions:** Formal analysis, L.C.; investigation, S.-A.W.; methodology, H.Z.; supervision, Z.W. and Y.A.; writing—original draft, S.-A.W.; writing—review and editing, S.-A.W., H.Z. and L.C. All authors have read and agreed to the published version of the manuscript.

**Funding:** This research was funded the National Key R&D Program of China (No. 2023YFC2205900, 2023YFC2205903), National Natural Science Foundation of China (N0. 52475249), National Natural Science Foundation of China (No. U21B2075), Reusable Space Debris Capture and Removal Project (N0. KJSP2020010302), Stable Supporting Fund of National Key Laboratory of Underwater Acoustic Technology (No. JCKYS2023604SSJS012), Fundamental Research Funds for the Central Universities (No. 3072023WD070101), and National Natural Science Foundation of China (No. 52375025).

**Data Availability Statement:** The data used to support the findings of this study are available from the corresponding author upon request.

**Conflicts of Interest:** The authors declare no conflicts of interest.

## References

1. Luo, J.; Bai, Y.Z.; Cai, L.; Cao, B.; Chen, W.M.; Chen, Y.; Cheng, D.-C.; Ding, Y.-W.; Duan, H.-Z.; Gou, X.; et al. The first round result from the TianQin-1 satellite. *Class. Quantum Gravity* **2020**, *38*, 185013. [CrossRef]
2. Zhang, D.X.; Ye, X.R.; Li, H.Y.; Zhao, G.Y.; Lian, J.X. Nonlinear modeling and validation of spacecraft dynamics for space-based gravitational wave detector. *Acta Astronaut.* **2024**, *224*, 57–68. [CrossRef]
3. Liu, Y.C.; Yan, H.; Zhou, Z.B. A single quasi-cubic test mass configuration for space-based gravitational wave detection. *Class. Quantum Gravity* **2023**, *40*, 015005. [CrossRef]

4. Gao, R.; Wang, Y.; Cui, Z.; Liu, H.; Liu, A.; Qian, X.; Wang, X.; Yao, Z.; Yang, Q.; Jia, J.; et al. On-ground demonstration of laser-link construction for space-based detection of gravitational waves. *Opt. Lasers Eng.* **2022**, *160*, 107287. [CrossRef]
5. Bailes, M.; Berger, B.K.; Brady, P.R.; Branchesi, M.; Danzmann, K.; Evans, M.; Holley-Bockelmann, K.; Iyer, B.R.; Kajita, T.; Katsanevas, S.; et al. Gravitational-wave physics and astronomy in the 2020s and 2030s. *Nature* **2021**, *2*, 344–366. [CrossRef]
6. Abbott, B.P.; Abbott, R.; Abbott, T.D.; Abraham, S.; Acernese, F.; Ackley, K.; Adams, C.; Adya, V.B.; Affeldt, C.; Agathos, M.; et al. A guide to LIGO-Virgo detector noise and extraction of transient gravitational-wave signals. *Nature* **2020**, *2*, 344–366. [CrossRef]
7. Martens, W.; Joffre, E. Trajectory Design for the ESA LISA Mission. *J. Astronaut. Sci.* **2021**, *68*, 402–443. [CrossRef]
8. Vallisneri, M. Synthetic LISA: Simulating time delay interferometry in a model LISA. *Phys. Rev. D* **2005**, *71*, 022001. [CrossRef]
9. Hartig ,M.; Wanner, G. Tilt-to-length coupling in LISA Pathfinder: Analytical modeling. *Phys. Rev. D* **2023**, *18*, 022008. [CrossRef]
10. Chen, Z.W.; Fang, C.; Wang, Z.P.; Yan, C.X; Wang, Z. The Influence of On-Orbit Micro-Vibration on Space Gravitational Wave Detection. *Photonics* **2023**, *10*, 908. [CrossRef]
11. Petiteau, A.; Anger, G.; Halloin, H.; Jeannin, O.; Plagnol, E.; Pireaux, S.; Regimbau, T.; Vinet, J.Y. LISACode: A scientific simulator of LISA. *Phys. Rev. D* **2008**, *77*, 023002. [CrossRef]
12. Huang, Z.Y.; Li, S.S.; Cai, L.; Fan, D.; Huang, L.Y. Estimation of the Center of Mass of GRACE-Type Gravity Satellites. *Phys. Rev. D* **2022**, *14*, 4030. [CrossRef]
13. Wei, X.T.; Huang, L.; Shen, T.Y.; Cai, Z.M.; He, J.B. Calibration of the in-orbit center-of-mass of TaiJi-1. *Phys. Rev. D* **2022**, *108*, 082001. [CrossRef]
14. Hua, L. *Study on Parameter Calibration of Eletrostatic Accelerometer During In-Flight Phase*; Harbin Institute of Technology: Harbin, China, 2009.
15. Wang, B.L.; Liao, H.; Han, Y. On-Orbit Calibration of Satellite Center of Mass Based on MME/EKF Algorithm. *Astronaut* **2010**, *31*, 2150–2156.
16. Xin, N.; Qiu, L.D.; Zhang, L.H.; Ding, Y.W.; Wang, D.L. Study on On-orbit Calibration of Center of Mass for Gravity Satellite. *Chin. Space Sci. Technol* **2013**, *33*, 9.
17. Bassan, M.; Cavalleri, A.; De Laurentis, M.; De Marchi, F.; De Rosa, R.; Di Fiore, L.; Dolesi, R.; Finetti, N.; Garufi, F.; Grado, A.; et al. Actuation crosstalk in free-falling systems: Torsion pendulum results for the engineering model of the LISA pathfinder gravitational reference sensor. *Astropart. Phys.* **2018**, *97*, 19–26. [CrossRef]
18. Hu, X.C.; Li, X.H.; Wang, Y.; Feng, W.F.; Zhou, M.Y.; Hu, YM.; Hu, S.C.; Mei, J.W.; Shao, C.G. Fundamentals of the orbit and response for TianQin. *Class. Quantum Gravity* **2018**, *35*, 095008. [CrossRef]
19. Zhang, H.; Xu, P.; Ye, Z.; Ye, D.; Qiang, L.E.; Luo, Z.; Qi, K.; Wang, S.; Cai, Z.; Wang, Z.; et al. A Systematic Approach for Inertial Sensor Calibration of Gravity Recovery Satellites and Its Application to Taiji-1 Mission. *Remote Sens.* **2023**, *15*, 3817. [CrossRef]
20. Meshksar, N.; Ferraioli, L.; Mance, D.; ten, Pierick, J.; Zweifel, P.; Giardini, D. Gravitational Reference Sensor Front-End Electronics Simulator for LISA. *J. Physics Conf. Ser.* **2017**, *840*, 012041. [CrossRef]